PNAS RESEARCH ARTICLE | CHEMISTRY

Dual-state stepwise methane-to-methanol conversion by water droplets with excellent yield and selectivity

Songtao Tang[a,1,2], Kejian Li[a,1], Jan Paul Menzel[b,c,1], Zhengwei Ye[a], Zhuoran Long[b,c], Kai Sun[d], Victor S. Batista[b,c,2], and Zetian Mi[a,2]

Affiliations are included on p. 9.

Edited by Michael Wasielewski, Northwestern University, Evanston, IL; received May 4, 2025; accepted November 30, 2025

Leveraging the continuous and rapid deposition and evaporation processes of water microdroplets on photocatalyst surfaces, this study presents an innovative dual-state stepwise methane conversion approach. This method significantly enhances the photocatalytic methane oxidation rate and selectivity, addressing the challenges of low methane solubility and poor liquid product selectivity typically found in aqueous-phase methane oxidation. By increasing the looping frequency per unit time, we achieved a state-of-the-art methane oxidation rate of 640 μmol g^{-1} h^{-1} using water as the sole oxidant, while maintaining approximately 95% selectivity toward liquid products, including 90% for methanol. This water microdroplet-assisted strategy not only establishes a framework for achieving both high yield and selectivity in photocatalytic methane oxidation but also pioneers a more efficient and sustainable approach for broadly applicable gases and water-involved photochemical conversion processes.

methane partial oxidation | hydrogen production | water microdroplets | dynamic wetting states | photocatalytic

Significance

Using water as an oxidant under solar illumination to convert methane into methanol while simultaneously producing hydrogen offers several benefits. This method reduces greenhouse effects, captures renewable solar energy, and produces high-purity hydrogen along with cost-effective methanol. However, selective methane conversion under mild conditions remains a grand challenge due to the low solubility of methane in water and the risk of overoxidation. To address limitations of conventional approaches, we developed a dual-state photocatalytic strategy, in which dynamic transitions between methane-rich and water-rich surface states, driven by water microdroplet deposition and evaporation, significantly enhance turnover frequency and product selectivity. This work provides a sustainable and scalable route for solar-driven methane upgrading.

Addressing greenhouse gas emissions and promoting renewable energy utilization are crucial to the sustainable development of human society. Methane, a major component of natural gas, is a potent greenhouse gas frequently released or flared due to high storage and transport costs. This underscores the urgent need for an efficient method to convert methane into transportable and valuable chemicals and fuels (1–3). N_2O and H_2O_2 are commonly used as oxidants for the partial oxidation of methane, but their high costs inhibit commercial applications (1, 2). Using oxygen to convert methane into liquid products results in an exothermic reaction that is unsuitable for capturing and storing renewable energy. In contrast, using water to convert methane into methanol is an endothermic reaction $(CH_4 + H_2O \rightarrow CH_3OH + H_2 \ \Delta H^{\circ}_{298} = 115.3 kJ/mol)$ (4). This conversion reaction not only harnesses renewable solar energy and mitigates greenhouse effects but also generates value-added liquid products alongside hydrogen. Notably, compared to photocatalytic overall water splitting, photocatalytic methane oxidation with water offers a highly sustainable approach for solar-to-chemical energy conversion.

Due to its nonpolar nature, methane exhibits extremely low solubility in water, which makes aqueous-phase methane oxidation often require high-pressure conditions (5, 6). Recently, photocatalysts with gas–liquid–solid triphasic interfaces are explored to improve CH_4 availability and enhance oxidation efficiency (7, 8). However, the catalyst surface treatment using hydrophobic materials (e.g., PTFE, polydimethylsiloxane, and Nafion) may cover active sites, inhibit charge carrier transfer, and suffer from instability issue (9–11). Additionally, the slow diffusion of partially oxidized products from triphasic interface into bulk solution and the direct mix with oxidants would result in overoxidation to undesired CO and/or CO_2 (2). A promising alternative is stepwise conversion, where methane reacts with oxygen from an activated carrier—typically the metal oxides—to produce desired products (12–17). This method does not require mutual solubility between reactants and achieves higher product selectivity by avoiding direct contact between intermediates and oxidants. For example, Sushkevich et al. employed a thermocatalytic stepwise approach to convert methane into methanol at high temperatures using water as the oxidant, achieving a selectivity of approximately 97% (15). Khodakov et al. highlighted a stepwise conversion of methane to ethane using a light-driven chemical looping strategy at ambient conditions, achieving over 90% selectivity (16). To date, the light-driven stepwise strategies for converting methane to liquid products, such as methanol, are still rarely explored. Moreover, in conventional stepwise conversion, each active site is limited to converting a single substrate molecule during each full catalytic cycle (15, 16). This limitation and the dead-time between each catalytic cycle results in a significantly lower catalytic turnover frequency (TOF) (or called space-time yield) compared to the

Author contributions: S.T. and Z.M. designed research; S.T., K.L., J.P.M., Z.Y., and K.S. performed research; S.T., J.P.M., Z.L., and V.S.B. analyzed data; and S.T., K.L., J.P.M., and Z.M. wrote the paper.

Competing interest statement: Some IP related to this work is licensed to NX Fuels, Inc., which was co-founded by Z.M. The University of Michigan and Mi have a financial interest in the company. The remaining authors declare no competing interests.

This article is a PNAS Direct Submission.

[1] S.T., K.L., and J.P.M. contributed equally to this work.

[2] To whom correspondence may be addressed. Email: songtat@illinois.edu, victor.batista@yale.edu, or ztmi@umich.edu.

This article contains supporting information online at https://www.pnas.org/lookup/suppl/doi:10.1073/pnas.2511126123/-/DCSupplemental.

continuous single-step conversion (12–19). The key to improving the TOF in stepwise conversion process lies in increasing the number of chemical cycles per unit time.

In this study, we proposed and demonstrated a dual-state stepwise methane conversion method, in which the catalyst surface alternates between anaerobic oxidation and catalyst reactivation through continuous transitions between dried (methane-rich) and wetted (water-rich) states by water microdroplets deposition and evaporation (Fig. 1*A*). By exploiting the rapid deposition and evaporation of water microdroplets on the photocatalyst surface, this dual-state methane conversion method resulted in a TOF of 226.4 h^{-1}, which is 400-fold and 100-fold higher than the aqueous-phase methane conversion and conventional stepwise methane conversion, respectively. The influences of water microdroplets deposition rate and light intensity on methane oxidation efficiency and product selectivity were also investigated. Furthermore, by using low-crystalline ZnO/Ag photocatalysts with easy oxygen vacancy (O_V) formation ability, we demonstrated a state-of-the-art methane oxidation rate of 640 μmol g^{-1} h^{-1} and a methane-to-methanol product selectivity of ~90%. This innovative synthetic approach, which utilizes the immiscibility of two reaction phases and the dynamic transitions of surface wetting

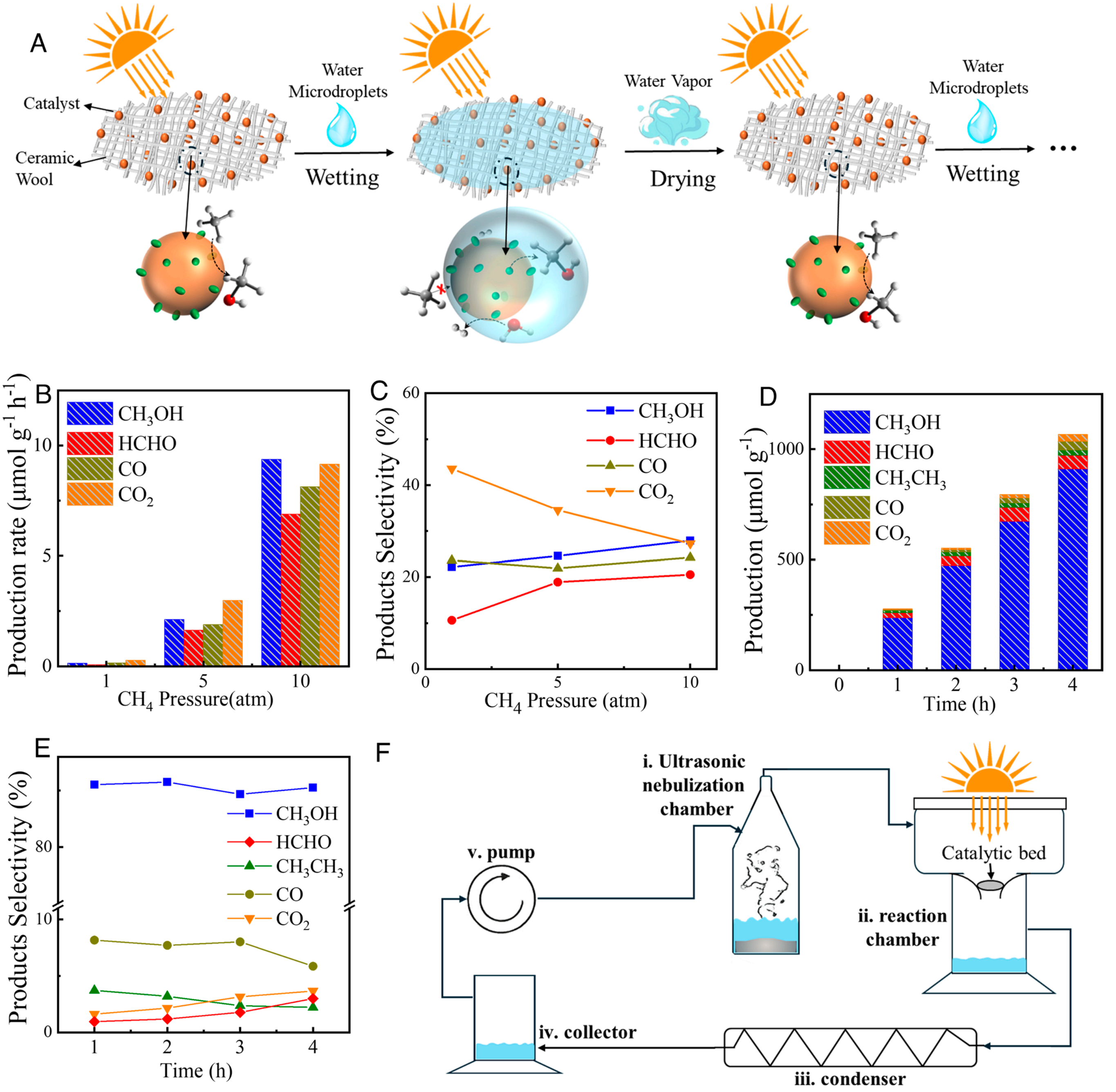

Fig. 1. Water microdroplet–assisted methane oxidation: concept, performance, and apparatus. (*A*) Concept of dual-state, water-droplet-assisted methane oxidation. Under sunlight, the catalyst surface alternates between wet (droplet-contact) and dry (postevaporation) states, enabling high activity and selectivity. (*B*) Product yields and (*C*) product selectivity at different methane pressures for aqueous-phase photocatalytic methane oxidation using bulk water as the sole oxidant (reaction time: 2 h). (*D*) Time-dependent product yields and (*E*) product selectivity for methane oxidation using water droplets as the oxidant (droplet deposition rate: 0.15 mL min^{-1}; light intensity: 15 suns). In all experiments (*B*–*E*), ZnO/Ag is used as the photocatalyst. (*F*) Schematic of the water microdroplet–assisted methane conversion apparatus. Gas circulates through (i) the ultrasonic nebulizer chamber, (ii) the reaction chamber, (iii) the condenser, (iv) the liquid collector, and (v) the circulation pump, returning to (i) to complete the cycle.

states, provides valuable guidance for enhancing reaction efficiency and product selectivity in photocatalytic methane conversion.

Results

Enhanced Photocatalytic Methane Oxidation with Water Microdroplets. At atmospheric pressure, the low solubility of methane in water limits its interaction with the catalyst (5, 6), significantly inhibiting the methane oxidation rate. Fig. 1 *B* and *C* show the product formation rate and the selectivity in aqueous phase photocatalytic oxidation under varying methane pressures with water as the sole oxidant. Silver-loaded zinc oxide (ZnO/Ag) was employed as the photocatalyst, which is fully dispersed in water. At 1 atm, the methane oxidation is nearly inert with a conversion rate of only 0.64 μmol g^{-1} h^{-1}. With increasing methane pressure in the reaction chamber, the methane oxidation rate increases to 8.61 μmol g^{-1} h^{-1} (5 atm) and 33.54 μmol g^{-1} h^{-1} (10 atm), owing to the enhanced solubility of methane in water. This, in turn, indicates that water acts as a barrier, preventing direct contact between methane and the photocatalyst. In this aqueous-phase reaction, the primary products are carbon monoxide and carbon dioxide with selectivity higher than 70%. This is because the intermediate products (such as methanol and formaldehyde) are highly susceptible to overoxidation when they contact with active radicals (such as hydroxyl radical) produced from water (20, 21). Therefore, promptly removing intermediate products from catalyst surface to control the methane oxidation process is important to achieve high yields and selectivity of liquid-phase value-added products.

Here, an approach for enhancing yield and selectivity of photocatalytic methane oxidation was developed by utilizing water microdroplets to replace bulk water. The apparatus for experiments is illustrated in Fig. 1*E* and *SI Appendix*, Figs. S1 and S2, which consisted of five parts: i) the ultrasonic nebulizer chamber, ii) the reaction chamber, iii) the condenser, iv) the liquid collector, and v) the circulation pump. In the atomization chamber, deionized water is atomized into ultrafine microdroplets with diameters of 5 to 20 μm using an ultrasonic nebulizer (*SI Appendix*, Fig. S3), then transported to the reaction chamber where they sprayed onto the catalyst surface. A water-cooled condenser tube condenses volatile products and water vapor, and the resulting condensate is routed to a downstream collector. Internal recirculation is driven by a diaphragm pump. The relative humidity in the reaction chamber maintained at 90 to 100% throughout the whole experiment, benefited from the continuous inlet of water microdroplets (*SI Appendix*, Fig. S4). The light source (irradiation intensity, 15 suns) irradiates the ceramic wool reaction bed loaded with ZnO/Ag photocatalyst. Fig. 1*C* exhibits the yield and time-dependent variations of oxidation products during methane photooxidation using water microdroplets as the oxidant. During the 4-h experiment, the yields of CH_3OH, HCHO, CO, CO_2, and C_2H_6 stably increased, along with an average methane oxidation rate of 278.6 μmol g^{-1} h^{-1}, which is significantly higher than that achieved under atmospheric pressure (0.64 μmol g^{-1} h^{-1}) and 10 atm pressure (33.5 μmol g^{-1} h^{-1}) in aqueous-phase methane oxidation. More importantly, this reaction mode achieved over 85% selectivity for methane-to-methanol conversion and over 90% selectivity for liquid-phase products (CH_3OH and HCHO), far exceeding that in aqueous-phase methane oxidation. In addition, as shown in *SI Appendix*, Fig. S5, under the identical experimental conditions, the hydrogen production also increased with illumination time increasing, exhibiting a similar evolution rate (250.2 μmol g^{-1} h^{-1}) to methane oxidation. The results clearly suggest that the use of water microdroplets can improve efficiency and selectivity of photocatalytic methane oxidation, which may be due to a distinct methane oxidation process compared to that in conventional aqueous phase reaction. Previous studies have reported methane oxidation occurring within microdroplets, nevertheless, the amount of oxidation products generated was minimal and the product selectivity was low (22).

In this study, when a UV-visible light filter (>850 nm) was used, only a minimal amount of carbon dioxide was detected (*SI Appendix*, Fig. S6), and the production of methanol was undetectable. Additionally, in the absence of catalysts or methane, almost no product was detected (*SI Appendix*, Fig. S6). These results verified that the generated products originate from photocatalytic methane oxidation.

To quantify light-to-chemical conversion, we measured monochromatic apparent quantum yield (AQY) from 350 to 450 nm (*SI Appendix*, Fig. S7*A*). ZnO/Ag exhibits a UV-dominated response, with the apparent quantum yield decreasing with wavelength and becoming negligible at 450 nm. A small residual at 405 nm likely arises from subbandgap/defect-tail states and/or Ag localized surface plasmon resonance assisted processes. The AQY values are 2.84% (350 nm), 2.40% (355 nm), 1.70% (365 nm), 0.46% (385 nm), 0.16% (405 nm), and 0% (450 nm); the corresponding light-to-chemical energy conversion efficiencies are 0.49%, 0.42%, 0.29%, 0.09%, 0.03%, and 0% (*SI Appendix*, Fig. S7*B*).

To assess stability of water microdroplet assisted methane oxidation, we performed long-duration, multicycle tests (six cycles; 24 h total). Both the methane oxidation rate and product selectivity remained highly stable across cycles (*SI Appendix*, Fig. S8 *A* and *B*). Pre- and posttest characterizations on ZnO/Ag catalyst show no discernible changes in surface chemical states, morphology, or crystallinity (*SI Appendix*, Fig. S8 *C–F*).

Dual-State Stepwise Methane Oxidation by Water Microdroplets. In aqueous-phase photocatalysis, the catalyst surface is in a wetting state at all time, making methane and the oxidation intermediates continuously interact with the oxidant (water molecules), thereby leading to severe overoxidation. In contrast, during the reaction processes involving water microdroplets, the photothermal effects could cause the microdroplets deposited on the catalyst surface to rapidly evaporate, driving the catalyst surface to repeatedly transition between wetted and dried states. *SI Appendix*, Fig. S9 shows the surface temperature changes of the catalyst-loaded reaction bed over time under illumination. *SI Appendix*, Fig. S10 illustrates the rapid microdroplet deposition and evaporation processes on the reaction bed surface, characterized using an infrared camera. Considering the strong shielding effect of water on methane to catalyst surface and its facilitation effect on liquid-phase product desorption (23), the surface reactions may differ under different wetting states. Fig. 2*A* illustrates the possible dual-state stepwise methane conversion process when using water microdroplets as oxidant. Specifically, when the catalyst surface is dry, the photocatalyst can directly contact methane in the gas phase and convert it into oxidized products by acting itself as an oxygen carrier (15). The oxidation process is essentially a gas–solid interface reaction, which can largely circumvent the low CH_4 availability issue in conventional aqueous phase reaction (24, 25). Subsequently, when the catalyst surface is enveloped by water microdroplets, the produced liquid products tend to detach from the catalyst surface, dissolve into the microdroplets, and leave the catalyst surface along with the evaporation. The water microdroplet–assisted rapid desorption of liquid products like methanol can suppress overoxidation and enable high selectivity (23). The vaporized droplets and liquid-phase products are directly taken away from the reaction chamber and subsequently condensed

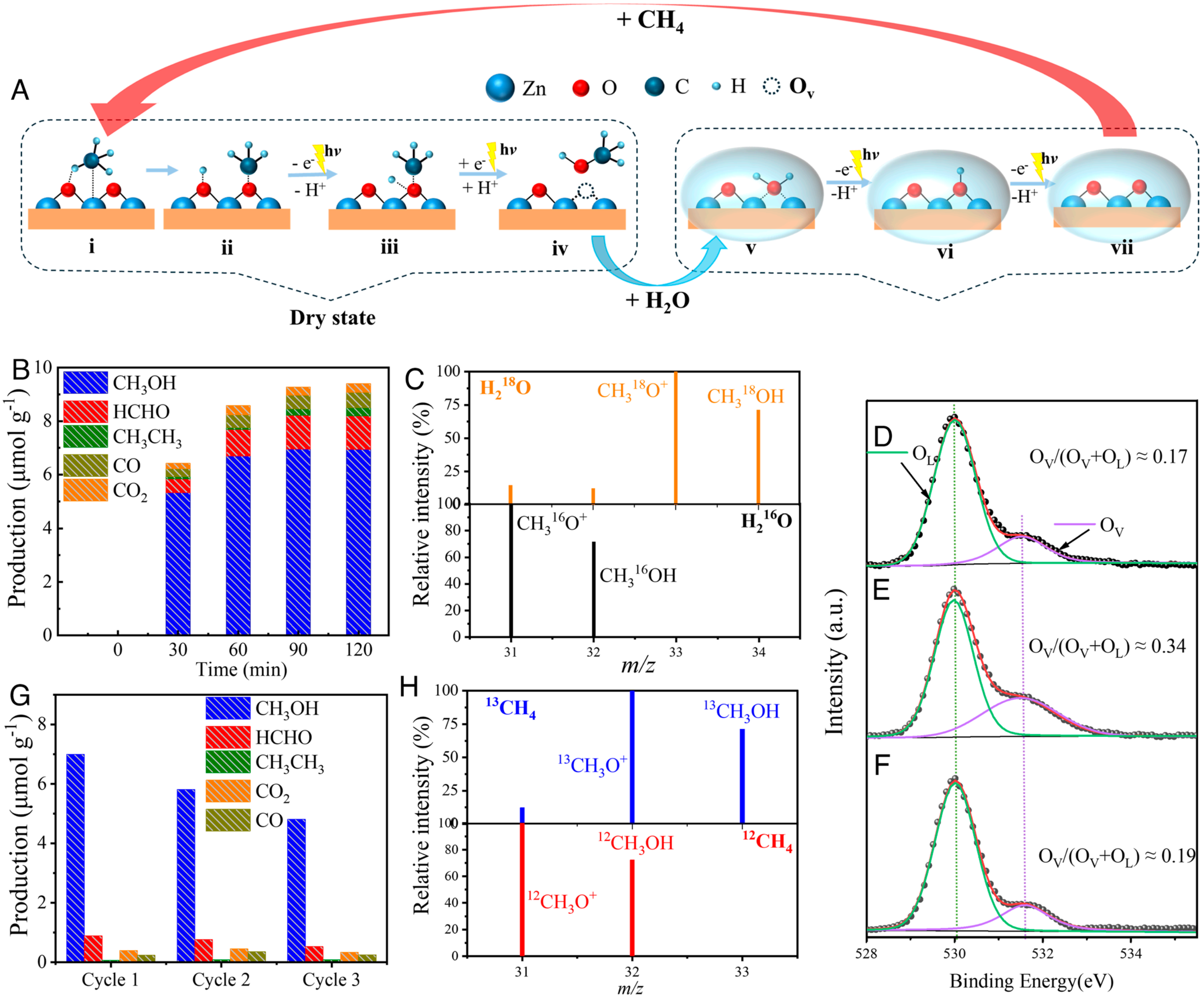

Fig. 2. (*A*) A schematic illustration of the possible reaction processes occurring on the catalyst surface in the dry and wet states during methane oxidation when using water microdroplets as the oxidant. The red (dry) and blue (wet) arrows indicate the alternating states. Dry state: (i) CH_4 adsorption; (ii) C–H activation; (iii) hole-driven oxidation of surface –OH, releasing proton; (iv) M–O bond scission to form CH_3OH and create oxygen vacancy. Wet: (v) H_2O adsorption at oxygen vacancy; (vi) H_2O dissociation/proton delivery; (vii) hole-driven –OH oxidation that replenishes lattice oxygen. (*B*) The evolution of products over time during anaerobic methane oxidation under illumination by an LED UV light at 355 nm. (*C*) GC-MS spectra of the products when $^{13}CH_4$ was used as the reactant instead of $^{12}CH_4$ in another anaerobic oxidation process. The O 1 s XPS spectra of ZnO/Ag (*D*) prior to the reactions, (*E*) after anaerobic methane oxidation (1st step), and (*F*) after the water reduction process (2nd step). (*G*) Methane oxidation rates and product selectivity in three cycles of conventional stepwise methane oxidation. (*H*) GC-MS spectra of the products formed during the second cycle (*Lower*) and the third cycle (*Upper*) of conventional stepwise methane oxidation.

and collected by the condenser, preventing further oxidation. At the same time, the methane-reduced catalytic sites on the catalyst surface in dry state, now covered by water microdroplets, could be reactivated by water under light excitation.

To verify our hypothesis, a conventional stepwise methane conversion experiment was conducted to simulate the reaction process (15–17, 19), as depicted in *SI Appendix*, Fig. S11. The stepwise methane conversion cycle involves an anaerobic methane oxidation process (1st step, without water), followed by a catalyst reactivation process using water (2nd step), which can simulate the reaction processes under dry and wet states in water microdroplet reaction system, respectively. Fig. 2*B* shows the yield of methane oxidation products over 2 h of reaction in the 1st step of the first cycle of conventional stepwise reaction. With prolonging the light irradiation time, the yields of oxidation products first increased and then gradually leveled off after 1.5 h likely due to the catalyst deactivation. To determine the carbon source of the oxygenates, we repeated the reaction using $^{13}CH_4$ (instead of $^{12}CH_4$) and analyzed the products by GC–MS. In the $^{12}CH_4$ control, the dominant ion is the molecular ion of $^{12}CH_3OH$ at m/z 32, accompanied by the fragment $^{12}CH_3O^+$ at m/z 31. In the $^{13}CH_4$ experiment, the base peak shifts to m/z 33, assigned to the molecular ion of $^{13}CH_3OH$; the ion at m/z 32 arises from the fragment $^{13}CH_3O^+$. The normalized relative intensity of 100% at m/z 33 confirms that the produced methanol carbon originates from CH_4 (Fig. 2*C*) (26). Due to the high volatility of formaldehyde and low concentration, no obvious molecular ion or fragment ion peaks of formaldehyde were observed in the GC-MS spectra. Furthermore, the selectivity for converting methane to liquid products in the first cycle reaches ~90% (Fig. 2*C*), which is significantly higher than that observed in aqueous-phase methane oxidation and similar to the results obtained when using water microdroplets as the oxidant. X-ray photoelectron spectroscopy (XPS) measurement was employed to investigate the changes in the surface chemical states of ZnO/Ag catalyst. Fig. 2 *D* and *E* show the O 1s XPS spectra of ZnO/Ag before and after anaerobic methane oxidation, respectively. The peak at approximately 530.2 eV corresponds to lattice oxygen (O^{2-}) in the ZnO crystal, while the peak at around 531.8 eV is associated with oxygen-related vacancies in the ZnO crystallographic structures (27–31). After anaerobic methane oxidation, the integral-area percentages of the peaks related to oxygen vacancies increased significantly from 0.17 to 0.34, indicating the increased oxygen vacancies in ZnO/Ag catalyst during anaerobic methane oxidation, which may be because the oxygen atoms in the photocatalyst participate methane oxidation.

Moreover, to complete the cycle of conventional stepwise methane oxidation, a catalyst reactivation process is conducted following the anaerobic methane oxidation process. Humidified argon is introduced into the reactor to remove unreacted methane and to fully wet the catalyst, simulating the wetting state of the catalyst during methane oxidation reactions using water microdroplets. Fig. 2*F* presents the O 1s XPS spectra of ZnO/Ag after 1 h of catalyst reactivation by water. The integral-area percentages of the peaks related to oxygen vacancies significantly decreased to 0.19. Then, in the second cycle reaction using the reactivated ZnO/Ag photocatalyst, we found the slightly reduced methane oxidation rate and selectivity compared to those observed in the first cycle, as shown in Fig. 2*G*. Nevertheless, the results indicate the successful reactivation of the ZnO/Ag catalyst in the presence of water molecules. Due to the separation of the oxidant from methane, zinc oxide cannot continuously supply oxygen for the deep oxidation of liquid products. As a result, the stepwise oxidation process achieves an average liquid products selectivity of ~87% in the anaerobic methane oxidation over three cycles, which is significantly higher than that observed in aqueous-phase oxidation (~30%) and closely resembling the selectivity obtained with the use of water microdroplets as the oxidant. To rule out interference from other potential oxidants, $H_2{}^{16}O$ was replaced with $H_2{}^{18}O$ during the water reduction process in the second cycle reaction. Fig. 2*H* shows the GC-MS spectra of the products formed during the second cycle (*Bottom*) and the third cycle (*Upper*). The peaks with m/z = 32 and 34 correspond to $CH_3{}^{16}OH$ and $CH_3{}^{18}OH$, respectively, while other peaks, such as $CH_3{}^{18}O^+$ (m/z = 33) and $CH_3{}^{16}O^+$ (m/z = 31), represent the ionized fragments. The $CH_3{}^{18}O^+$ peak at m/z = 33 appears with 100% relative intensity (orange line, Fig. 2*H*) in the third cycle reaction, demonstrating that the oxygen in the methanol originates from H_2O that participated in ZnO/Ag reactivation. In subsequent cycles (cycle 4 to cycle 6, *SI Appendix*, Fig. S12), the photocatalytic methane oxidation under anaerobic condition in stepwise oxidation system showed stable performances, further indicating that the use of water molecules can successfully reactivate the ZnO/Ag photocatalyst through filling oxygen vacancies. In the initial three cycles, the decline in catalyst performance may be attributed to the irreversible or partially reversible reconstruction, sintering, or deactivation of some active sites (32–34). As the number of cycles increases, a dynamic equilibrium of oxygen species is established on the catalyst surface, thereby stabilizing the catalytic performance. Notably, during the photocatalyst reactivation period, a specific quantity of hydrogen was produced from the reduction of water, as shown in *SI Appendix*, Fig. S13, which supports the crucial role of water molecules in catalyst reactivation via contributing the oxygen atoms.

Compared to the use of humidified argon for transitioning the ZnO/Ag catalyst from anaerobic oxidation to the reactivation mode in the conventional stepwise reaction system, the rapid wetting and evaporation of water microdroplets on the catalyst surface facilitates high-frequency stepwise conversion (*SI Appendix*, Fig. S10). When both the light intensity and water microdroplets deposition rate are optimum, the water microdroplets deposited on the ZnO/Ag surface have sufficient time to restore the deactivated catalytic sites and can be promptly removed through the photothermal effects caused by the incident light. We then investigated the effects of water microdroplet evaporation and deposition rate on methane photooxidation, which was controlled through varying water deposition rate and light irradiation intensity: 1) the higher the water deposition rate, the faster the deposition and the slower evaporation of water droplets, and 2) the higher light intensity, the faster evaporation of water droplets. *SI Appendix*, Fig. S9 illustrates the increased stable surface temperature of the catalyst-loaded reaction bed as a function of light intensity, where the higher temperatures will increase evaporation rates. Fig. 3 *A* and *B* illustrate the methane oxidation rate and its selectivity toward liquid products under varying water microdroplet deposition rates and light intensity levels, respectively. When the water microdroplets deposition rate is approximately 0.15 mL/min and the light intensity is around 15 suns, the ZnO/Ag photocatalyst achieves a maximum methane oxidation rate of 280 μmol g^{-1} h^{-1} and a methanol selectivity of ~90%. This dual-state stepwise conversion allows catalytic sites to undergo repeated utilization within a short time, substantially enhancing the turnover frequency of the catalyst and enabling significantly higher catalytic rates. A TOF of 226.4 h^{-1} is achieved at a water deposition rate of 0.15 mL/min and a light intensity of 15 suns, which is over 400 and 100 times higher than that of aqueous-phase methane conversion under atmospheric pressure (0.55 h^{-1}) and conventional stepwise conversion (an average value of 2.07 h^{-1} in the first three cycles), as shown in *SI Appendix*, Fig. S14.

At high microdroplet deposition rates, the catalyst remains constantly in the wetting state, where the surface environment is similar to that of methane oxidation in aqueous phase at atmospheric pressure. In this case, the oxidation rate is primarily constrained by the concentration of methane dissolved in water rather than the light irradiation intensity. As shown in Fig. 3 *A* and *B*, when the water microdroplet deposition rate exceeds 0.7 mL/min, variations in light intensity have insignificant impact on the methane oxidation rate, and the selectivity for liquid products is low. When the light intensity is too high and the water microdroplet deposition rate is relatively low, the evaporation rate exceeds the water deposition rate, leading to the catalyst being predominantly in dry state. Under this condition, the consumed catalytic sites are unable to undergo timely reactivation by water, thereby causing a decrease in oxidation activity.

To further interrogate the dry–wet dual-state mechanism, we measured both reaction orders and apparent activation energies. At fixed photon flux, we independently varied the methane partial pressure and the microdroplet deposition rate. The fitted reaction orders are $\alpha = 0.77$ for CH_4 and $\beta = 0.98$ for microdroplets deposition rate (*SI Appendix*, Fig. S15 *A* and *B*). The fact that $\beta > \alpha$ indicates that wet-side processes exert stronger kinetic control than further increases in CH_4 under our conditions. Because the surface inherently cycles between wet contact and a postevaporation dry state, determining a purely "wet" or purely "dry" apparent activation energy is impractical. At an appropriate droplet deposition rate, increasing the catalyst-surface temperature shortens droplet residence and enlarges the dry fraction, whereas decreasing temperature does the opposite. Accordingly, by keeping the deposition rate fixed and measuring the apparent activation energy in two temperature windows—a dry-biased high-temperature window (100 to 120 °C) and a wet-biased low-temperature window (65 to 85 °C)—we can thereby further examine the existence of the

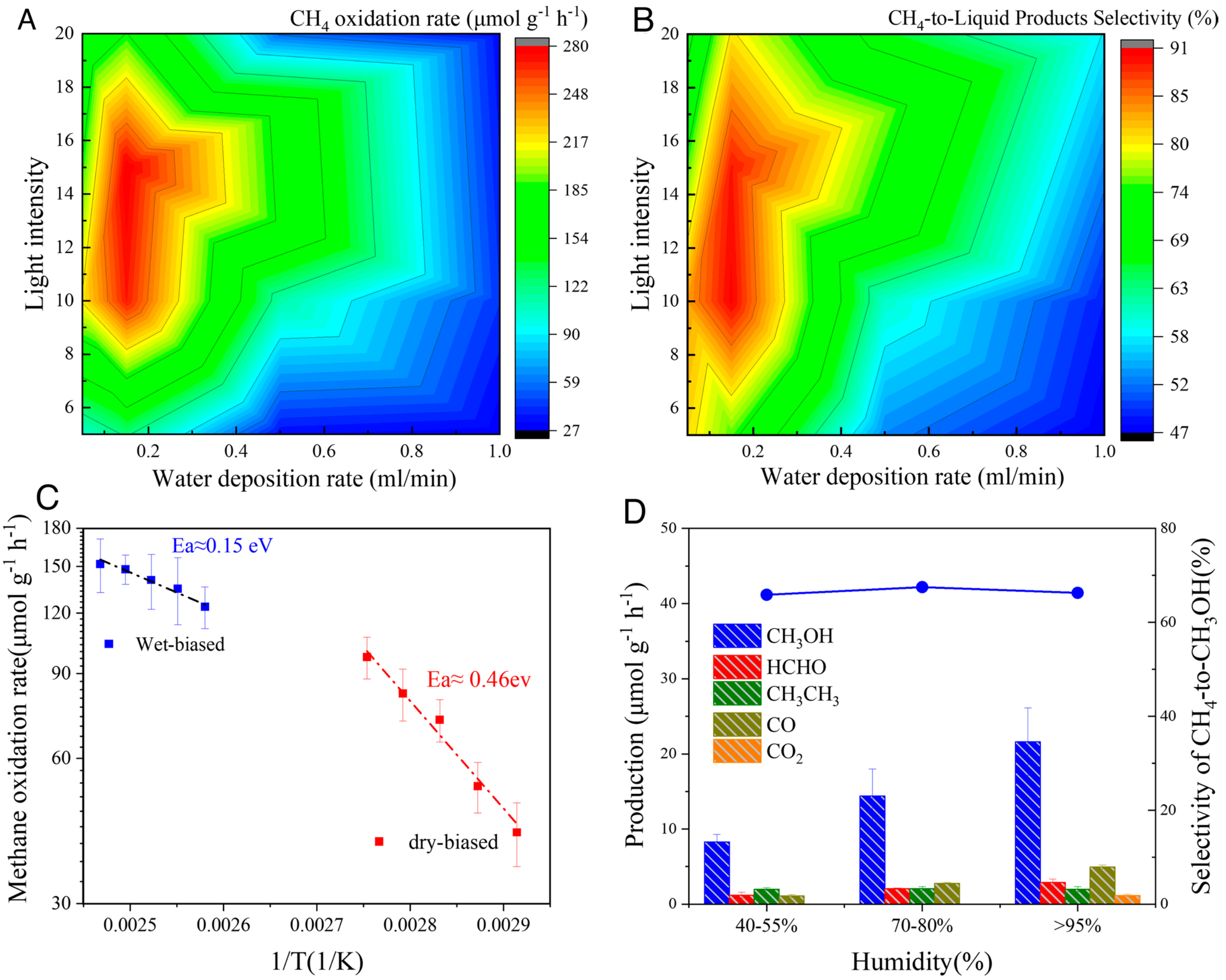

Fig. 3. (*A*) Methane oxidation rate and (*B*) methane-to-liquid product selectivity under various water deposition rates and light intensity levels. (*C*) Arrhenius plots (Log_{10}(rate) vs. 1/T) in two temperature windows at fixed J_w: the blue fit (100 to 120 °C) yields the dry-biased apparent activation energy $E_{a,\text{dry-biased}}$; the red fit (65 to 85 °C) yields the wet-biased $E_{a,\text{wet-biased}}$. (*D*) Product formation rates and selectivity for CH_4 oxidation in humidity control experiments with no droplets (CH_4 + water vapor cofeed), highlighting the contrast with the droplet-enabled pathway.

dual-state reaction. The apparent activation energies are 0.15 eV in the dry-biased window and 0.46 eV in the wet-biased window (Fig. 3*C*). The clear difference between the two activation energies further provides kinetic evidence for a coupled dual-state cycle.

To isolate ambient-humidity effects, we performed humidity-only controls in which CH_4 was prehumidified, but no microdroplets were introduced. Both total yields and methanol selectivity dropped markedly: Even at RH > 95%, the methane oxidation rate plateaued at ~30 μmol g^{-1} h^{-1} and methanol selectivity at ~65% (Fig. 3*D*). Compared with the conventional stepwise methane conversion (Fig. 2), cofeeding methane with water vapor drives fragile intermediates to further overoxidation. Under high humidity, this direct methane oxidation can occur concomitantly during our microdroplet-assisted stepwise process, likely explaining why 100% methanol selectivity is not achieved.

Enhanced Performance by Promoting O_V Formation. In addition to the deposition and evaporation rates of water microdroplets, the formation of oxygen vacancies on the catalyst surface also plays a crucial role in methane anaerobic photocatalytic oxidation. The reason for selecting zinc oxide as the oxygen carrier here is that, compared to other oxides, it has a lower surface oxygen vacancy formation energy (20). The introduction of metal cocatalysts lowers the formation energy of oxygen vacancies and serves as an electron reservoir, thereby enhancing photoinduced charge-carrier separation and facilitating proton transfer (35, 36). As shown in Fig. 4*A*, ZnO/Ag, ZnO/Au, and ZnO/Pt—ZnO loaded with highly electronegative metal cocatalysts—exhibit similar methane oxidation activities in experiments using water microdroplets, significantly outperforming ZnO catalyst. The results demonstrated the important roles of oxygen atoms of oxides in dual-state stepwise methane oxidation. Materials with low crystallinity or amorphous structures tend to exhibit easier oxygen vacancies formation compared to perfect crystals (37, 38). Here, ZnO/Ag catalysts with lower crystallinity were synthesized for further enhancing the methane oxidation rate. By immersing the materials in an ammonium hydroxyzincate solution and controlling the drying temperatures, low-crystallinity ZnO/Ag samples (denoted as LC-ZnO/Ag-1 and LC-ZnO/Ag-2, larger suffix numbers indicate the use of higher concentrations of ammonium hydroxyzinate solutions) were successfully prepared. *SI Appendix*, Fig. S16 shows the X-ray diffraction (XRD) spectra of ZnO/Ag, LC-ZnO/Ag-1, and LC-ZnO/Ag-2 samples. The full width at half maximum

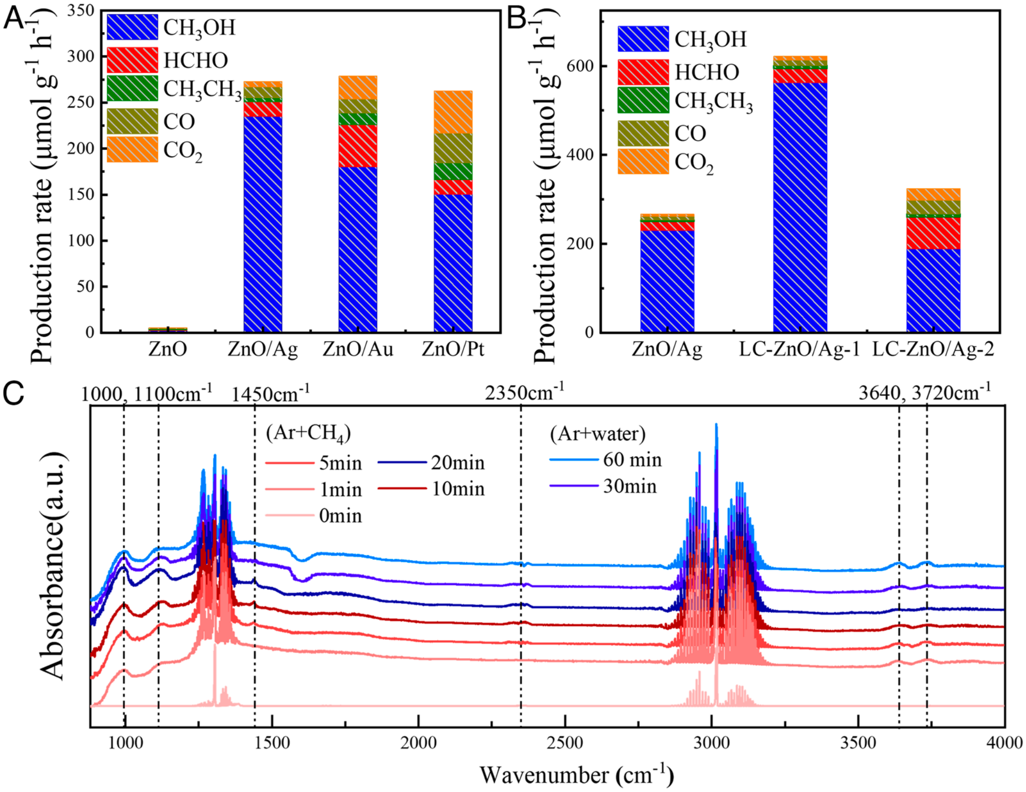

Fig. 4. Methane oxidation rate and product distribution obtained from experiments using water microdroplets as the oxidant with the use of (*A*) ZnO photocatalysts featuring various cocatalysts and (*B*) ZnO/Ag photocatalysts of differing crystallinities. (*C*) DRIFTS spectra recorded during stepwise oxidation in oxygen-free chamber under CH_4/Ar and H_2O/Ar environments. For the first 30 min, only CH_4/Ar was purged into the reaction chamber, followed by the introduction of H_2O/Ar.

(FWHM) of the (101) peak increases from the 0.22° 2θ (ZnO/Ag) to 0.26° 2θ (LC-ZnO/Ag-1) and 0.33° 2θ (LC-ZnO/Ag-2), indicating a decrease in crystallinity after ammonium hydroxyzincate treatment. The high-angle annular dark-field (HAADF) scanning transmission electron microscopy (STEM) images of ZnO/Ag and LC-ZnO/Ag-1 are shown in *SI Appendix*, Fig. S17. The ZnO/Ag sample exhibits a smooth surface with continuous and uniform lattice fringes. As a portion of zinc oxide dissolves into the ammonium hydroxyzincate solution and subsequently recrystallizes during the drying and crystallization process, the surface of the LC-ZnO/Ag-1 sample exhibits increased roughness and intermittent lattice fringes. Fig. 4*B* shows the performance of these samples in methane oxidation reaction using water microdroplets as oxidant. It can be observed that the LC-ZnO/Ag-1 and LC-ZnO/Ag-2 exhibit higher methane oxidation rates compared to ZnO/Ag. At ambient pressure (1 atm), using the dual-state strategy, LC-ZnO/Ag-1 achieved a state-of-the-art methane oxidation rate of ~640 μmol g^{-1} h^{-1} and a comparable liquid-product selectivity of ~95% (≈90% methanol), as shown in *SI Appendix*, Fig. S18 and Table S1. Regions with low crystallinity are prone to significant recombination of photogenerated charge carriers, impeding the efficient transfer of photogenerated electrons and holes to catalytic sites for reaction (39). Consequently, LC-ZnO/Ag-2 demonstrates a reduced methane oxidation rate compared to LC-ZnO/Ag-1. The improvement may also likely arise from the increased exposure of polar facets (40), which reduces the formation energy of oxygen vacancies and thereby enhances activity. Irrespective of the precise origin, the observed trend accords with a Mars–van Krevelen–type mechanism—namely, higher activity results from a lowered oxygen-vacancy formation energy.

To assess the generality of the dual-state strategy, we evaluated CeO_2/Ag, TiO_2/Ag, and g-C_3N_4/Ag (*SI Appendix*, Fig. S19). With microdroplet assistance, oxide photocatalysts showed marked gains over the conventional high-pressure aqueous system: CeO_2/Ag delivered ~200 μmol g^{-1} h^{-1} with ~89% liquid-product selectivity, and TiO_2/Ag reached ~100 μmol g^{-1} h^{-1} with ~85% selectivity. The lower activity of TiO_2/Ag likely reflects its higher oxygen-vacancy formation energy (20), whereas g-C_3N_4/Ag showed no clear enhancement, consistent with the absence of lattice oxygen.

Methane Oxidation Catalytic Mechanisms Investigation. Furthermore, the in situ diffuse reflectance FTIR (DRIFTS) measurements were employed to track the methane oxidation process. The DRIFTS experiments were conducted in a dry and oxygen-free chamber under CH_4/Ar or H_2O/Ar atmosphere. During the first 30 min, only the CH_4/Ar mixture was purged into the reaction chamber to simulate the anaerobic catalytic process under dry conditions. As illustrated in Fig. 4*C*, the spectra obtained in dark exhibit only two prominent peaks at 1,303 cm^{-1} and 3,010 cm^{-1}, corresponding to gaseous CH_4 (41). Upon 1 min of illumination, peaks near 1,100 and 1,050 cm^{-1} appeared, corresponding to the C—O stretching vibrations of the methoxy species from adsorbed methanol (CH_3OH_{ads}) (42, 43). The peak at around 1,450 cm^{-1} is attributed to the C—H bending vibration mode of adsorbed methanol molecules (CH_3OH_{ads}) (44, 45). With illumination time increasing, two additional characteristic peaks were observed at 2,350 cm^{-1} and 1,590 cm^{-1}, corresponding to the C═O stretching vibration of formaldehyde and the asymmetric stretching vibration of CO_2, respectively. This indicates that methanol acts as an intermediate product in the oxidation of methane, leading to the formation of formaldehyde, carbon monoxide, and carbon dioxide. After 30 min of photocatalysis reaction, the CH_4/Ar flow was replaced with H_2O/Ar to investigate the role of water molecules in the dual-state stepwise conversion under wetting conditions. A rapid decrease in the methanol-related peaks was observed, validating the desorption effect of water vapor on methanol. Furthermore, peaks at approximately 3,640 cm^{-1} and 3,720 cm^{-1} in the high wavenumber region, attributed to surface hydroxyl groups (15, 46, 47), diminished rapidly under CH_4/Ar flow but were restored under H_2O/Ar flow.

Using DFT, we performed a mechanistic study to propose a possible methane oxidation mechanism (computational details can be found in the *SI Appendix*). In Fig. 5, we display the relative Gibbs free energy of each respective intermediate, with the optimized geometries given in Fig. 5*B*, including reaction free energies of each step. We chose the polar ZnO(0001) surface, one of the most dominant low-index surfaces, to model the oxygen-rich ZnO (48). We have also investigated the nonpolar ZnO(10 − 1 0) surface (*SI Appendix*, Fig. S22), which however showed endergonic methane dissociative adsorption, which suggests low contribution to the overall catalytic activity. However, on the oxygen-terminated polar surface, dissociation of the methane is heavily exergonic (−2.56 eV), leading to a methyl radical (•CH_3) attached on the surface and a hydroxyl radical integrated into the surface, an intermediate we call ZnO*CH_3_ZnO*H. Upon photoexcitation, the surface integrated hydroxyl group gets oxidized by photogenerated holes, releasing a proton (+1.47 eV, provided by the high-energy photogenerated holes), leading to the ZnO*CH_3 intermediate. When the formation energy of oxygen vacancies is low, the O*•CH_3 radicals can break the oxygen–metal bonds under light excitation, by reduction through photogenerated holes and subsequent reprotonation, leading to methanol formation while simultaneously generating oxygen vacancies on the zinc oxide surface (+0.77 eV, easily provided by high-energy electrons generated by photoexcitation) (20, 40). This process corresponds to the decrease in hydroxyl intensity during the CH_4/Ar flow observed in Fig. 4*C*. The removal of surface oxygen leads to deactivation of the catalytic sites, thus preventing further oxidation of the generated methanol and ensuring high methanol selectivity during anaerobic methane oxidation. When the catalyst surface becomes wetted, the generated oxygen vacancies are replenished by water, under release of a proton and photooxidation, this leads to the ZnO*H intermediate (−0.44 eV). This is also experimentally evidenced by the increase in hydroxyl group intensity in Fig. 4*C* during the H_2O/Ar flow. Further oxidation of this intermediate leads to the ZnO surface (+1.93 eV), regenerating the catalyst and allowing for the next catalytic cycle.

It is important to note that the reaction under dry condition is stochiometric with regard to photoexcited electrons and holes as well as protons, while under wet conditions, electrons and protons are generated. Accumulation of electrons at the Ag (or other metal cocatalyst) nanoparticles and abundance of protons then leads to hydrogen evolution on the silver site (49, 50), extracting the excess electrons and holes. This therefore leads to the following reaction equations under dry and wet conditions:

$$CH_4 + ZnO \overset{h\nu}{\rightarrow} CH_3OH + ZnO_v \text{ Dry},$$

$$ZnO_v + H_2O \overset{h\nu}{\rightarrow} ZnO + 2H^+ + 2e^- \text{ Wet},$$

$$CH_4 + H_2O \overset{h\nu}{\rightarrow} CH_3OH + 2H^+ + 2e^- \text{ (Total).}$$

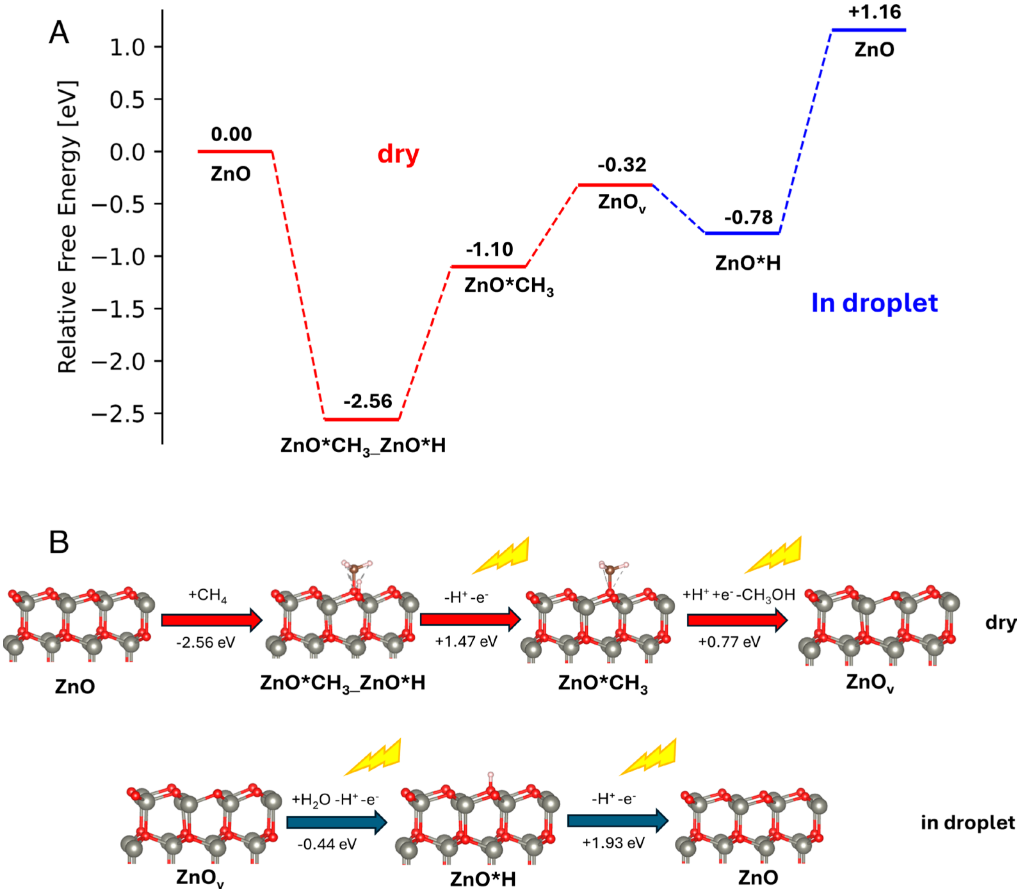

Fig. 5. Proposed mechanism of photocatalytic methane oxidation to methanol. (*A*) Free energy profile including each respective reaction intermediate. (*B*) Optimized geometries and free energies of reaction for the reaction steps.

With the reduction on silver (or other metal cocatalyst):

$$2H^+ + 2e^- \xrightarrow{h\nu} H_2.$$

This leads to the total reaction equation

$$CH_4 + H_2Oh\nu - CH_3OH + H_2.$$

Discussion

In summary, this study presents a photocatalytic method for converting methane into high-valued liquid product, CH_3OH, using water microdroplets as the sole oxidant, with metal-loaded low-crystallinity zinc oxide acting as the oxygen carrier. We propose a dual-state stepwise methane conversion model in the presence of water microdroplets, supported by complementary evidence from kinetics, isotopic labeling with XPS, DFT calculation, and in situ DRIFTS. In this reaction mode, the rate of methane oxidation and the selectivity of products can be adjusted by controlling the deposition and evaporation rates of water microdroplets. This dual-state stepwise oxidation method overcomes the low catalytic turnover frequency (TOF) of conventional stepwise conversion and the poor product selectivity in atmospheric aqueous-phase reactions. It simultaneously achieves a high methane oxidation rate (640 μmol g^{-1} h^{-1}) and excellent selectivity (~95%) for liquid products (CH_3OH and HCHO). This study offers an efficient stepwise conversion strategy for photocatalytic methane upgrading.

Materials and Methods

Materials Preparation. Ag-loaded photocatalysts (Ag/ZnO as the primary system; Ag/CeO_2, Ag/TiO_2, and $Ag/g\text{-}C_3N_4$ for generality) were prepared by a photodeposition procedure: A suspension of the support (ZnO, TiO_2, CeO_2, $g\text{-}C_3N_4$) in H_2O/MeOH containing $AgNO_3$ was evacuated and irradiated with a Xe lamp (30 min), then washed and vacuum-dried at 60 °C. To obtain low-crystalline ZnO shells, crystalline ZnO/Ag powders were contacted with ammonium hydroxyzincate solution, rapidly filtered, and vacuum-dried at 90 °C to dehydrate hydroxyzincate to a ZnO overlayer; Ag was then redeposited by the same photodeposition step. Full reagent amounts and step-by-step conditions are provided in *SI Appendix*, section S1.

Methane Oxidation Experiments. Three reaction modes were employed. i) Aqueous high-pressure tests: 100 mg catalyst was dispersed in 20 mL H_2O in a 150 mL stainless-steel reactor (PTFE liner, quartz window) and irradiated with a 300 W Xe lamp (~15 suns) after Ar/Methane purging; typical reaction time was 2 h. ii) Conventional stepwise mode: ~200 mg catalyst on a ceramic-wool bed in a 30 mL glass reactor was dried/degassed, exposed to CH_4/Ar (1:3) under illumination for the anaerobic oxidation step, then reactivated by humid Ar/H_2O flow; liquids and gases were collected after each cycle. iii) Microdroplet-assisted dual-state mode: Deionized water was atomized into ultrafine microdroplets and delivered to the illuminated catalyst bed (300 W Xe, quartz window) using a sealed internal-circulation apparatus; condensate and gas-phase products were captured downstream via condenser/collectors. Detailed operating procedures and the design of the microdroplet-assisted methane oxidation apparatus are provided in the *SI Appendix*, sections S2 and S3.

Product Analysis. Gaseous and liquid products were quantified using complementary methods. Gas products (CH_4, CO, CO_2, H_2) were analyzed on a GC equipped with TCD and FID. Liquid products were first screened by ^1H NMR (D_2O; maleic acid internal standard) and then quantified by GC-FID with external-standard calibration. Formaldehyde was determined by the acetylacetone (Nash) colorimetric method after derivatization (60 °C, 10 to 30 min; absorbance at 413 nm). Isotopic incorporation from $^{13}CH_4$ or $H_2{}^{18}O$ was verified by GC-MS from methanol mass shifts. Details are provided in the *SI Appendix*, section S7.

Kinetic and Activation-Energy Measurements. Kinetic tests were performed in the same sealed internal-circulation reactor and protocol as standard runs (total pressure 1 atm; illumination 10 suns). The methane order (α) was obtained with the droplet flux J_w fixed ($\approx$0.15 mL min^{-1}) while varying P_{CH4} from 0.1 to 1.0 atm (Ar balance); α equals the slope of $\log_{10}$(rate) vs. $\log_{10}P_{CH4}$. The droplet order (β) was measured with P_{CH4} fixed (0.7 atm) while varying J_w from 0.05 to 0.15 mL min^{-1}; β equals the slope of $\log_{10}$(rate) vs. $\log_{10}J_w$. Apparent activation energies were determined by replacing the ceramic-wool bed with a PID-heated circular quartz disk bearing a drop-cast catalyst film (areal loading $\approx$ 64 mg cm^{-2}) and irradiated by a 365 to 385 nm UV-A LED (~85 mW cm^{-2}); at fixed J_w (~0.1 mL min^{-1}) we swept the disk temperature to define wet-biased (65 to 85 °C) and dry-biased (100 to 120 °C) windows and constructed Arrhenius plots separately to obtain $E_{a,wet}$ and $E_{a,dry}$. Full operating conditions, instrumentation, and regression procedures are provided in *SI Appendix*, sections S5 and S6.

Apparent Quantum Yield and Light-to-Chemical Energy Calculation. AQY(λ) was measured under monochromatic LEDs (350 to 450 nm); a >800 nm-filtered Xe lamp supplied only thermal input for droplet evaporation, and its photons were not counted. AQY(λ) equals electron-weighted product moles divided by incident photons, and the methanol light-to-chemical efficiency is calculated as

$$\eta_{LCEE}(\lambda) = \mathrm{AQY}_{CH_3OH}(\lambda)\frac{\Delta G_{net}}{2h\nu},$$

where hν is the photon energy. The factor of two accounts for the two-electron process associated with CH_3OH formation. More details are provided in *SI Appendix*, section S8.

Materials Characterization and In situ DRIFTS. Catalysts were characterized by STEM, XPS, PL, and XRD (instrument models and settings in SI). In situ DRIFTS was performed on a Bruker FT-IR under anaerobic conditions: The catalyst on a quartz-disk was pretreated in Ar at 100 °C for 30 min, then exposed to CH_4/Ar (1:5, 5 sccm) for 1 h, illuminated for 30 min, and finally switched to H_2O/Ar for 20 min. (*SI Appendix*, section S11).

Computational Methods. Surface models included polar O-terminated ZnO(0001) and nonpolar (100) slabs (four double layers; top and bottom layers relaxed; 30 Å including vacuum). A detailed description of the DFT-based computational methods, model construction, associated references, as well as complete model definitions and tabulated energies and free energies, is provided in the *SI Appendix*, Figs. S20–S22, Table S2–S4, and section S12.

Data, Materials, and Software Availability. Study data are included in the article and/or *SI Appendix*.

ACKNOWLEDGMENTS. We gratefully acknowledge the research support from the US Army Research Office under contract No. W911NF2110337. The TF Spectra 300 and TF Helios Xe PFIB instruments were operated by Michigan Center for Materials Characterization under support by the University of Michigan.

Author affiliations: [a]Department of Electrical Engineering and Computer Science, University of Michigan, Ann Arbor, MI 48109; [b]Department of Chemistry, Yale University, New Haven, CT 06520-8107; [c]Energy Sciences Institute, Yale University, West Haven, CT 06516; and [d]Department of Materials Science and Engineering, University of Michigan, Ann Arbor, MI 48109

1. P. Schwach, X. L. Pan, X. H. Bao, Direct conversion of methane to value-added chemicals over heterogeneous catalysts: Challenges and prospects. *Chem. Rev.* **117**, 8497–8520 (2017).
2. X. Y. Li, C. Wang, J. W. Tang, Methane transformation by photocatalysis. *Nat. Rev. Mater.* **7**, 617–632 (2022).
3. R. W. Howarth, R. Santoro, A. Ingraffea, Methane and the greenhouse-gas footprint of natural gas from shale formations: A letter. *Clim. Change* **106**, 679–690 (2011).
4. M. Bertau, H. Offermanns, L. Plass, F. Schmidt, H.-J. Wernicke, *Methanol: The Basic Chemical and Energy Feedstock of the Future* (Springer, 2014), vol. 1.
5. S. Yamamoto, J. B. Alcauskas, T. E. Crozier, Solubility of methane in distilled water and seawater. *J. Chem. Eng. Data* **21**, 78–80 (1976).
6. C. G. Pruteanu, G. J. Ackland, W. C. K. Poon, J. S. Loveday, When immiscible becomes miscible-Methane in water at high pressures. *Sci. Adv.* **3**, e1700240 (2017).
7. C. He *et al.*, Photocatalytic conversion of methane to ethanol at a three-phase interface with concentration-matched hydroxyl and methyl radicals. *J. Am. Chem. Soc.* **146**, 11968–11977 (2024).
8. A. Thakur, K. Chauhan, A. Kumar, Triphase photocatalysis: Beyond conventional diphase photocatalytic reactions. *Small* **21**, 2501329 (2025).

9. H. Zhou *et al.*, Increasing the efficiency of photocatalytic reactions via surface microenvironment engineering. *J. Am. Chem. Soc.* **142**, 2738–2743 (2020).
10. R. Shi *et al.*, Efficient wettability-controlled electroreduction of CO_2 to CO at Au/C interfaces. *Nat. Commun.* **11**, 3028 (2020).
11. H. Chen *et al.*, Surface redox chemistry regulates the reaction microenvironment for efficient hydrogen peroxide generation. *J. Am. Chem. Soc.* **146**, 15356–15365 (2024).
12. J. Zhu *et al.*, Phase distribution and stepwise kinetics of iron oxides reduction during chemical looping hydrogen generation in a packed bed reactor. *Int. J. Hydrogen Energy* **40**, 12097–12107 (2015).
13. M. Ravi *et al.*, Misconceptions and challenges in methane-to-methanol over transition-metal-exchanged zeolites. *Nat. Catal.* **2**, 485–494 (2019).
14. W. T. Zheng, K. Q. Sun, H. M. Liu, Y. Liang, B. Q. Xu, Nanocomposite Ni/ZrO_2: Highly active and stable catalyst for H_2 production via cyclic stepwise methane reforming reactions. *Int. J. Hydrogen Energy* **37**, 11735–11747 (2012).
15. V. L. Sushkevich, D. Palagin, M. Ranocchiari, J. A. van Bokhoven, Selective anaerobic oxidation of methane enables direct synthesis of methanol. *Science* **356**, 523–525 (2017).
16. X. Yu *et al.*, Stoichiometric methane conversion to ethane using photochemical looping at ambient temperature. *Nat. Energy* **5**, 511–519 (2020).
17. S. E. Bozbag *et al.*, Direct stepwise oxidation of methane to methanol over Cu-SiO_2. *ACS Catal.* **8**, 5721–5731 (2018).
18. Z. J. Wang *et al.*, Mass transfer modulation by hollow multi-shelled structures for high space-time yield synthesis of light olefins from syngas. *Adv. Funct. Mater.* **34**, 2316547 (2024).
19. S. Chuayboon, S. Abanades, S. Rodat, Stepwise solar methane reforming and water-splitting via lattice oxygen transfer in iron and cerium oxides. *Energy Technol.* **8**, 1900415 (2020).
20. C. Q. Han *et al.*, Selective cleavage of chemical bonds in targeted intermediates for highly selective photooxidation of methane to methanol. *J. Am. Chem. Soc.* **145**, 8609–8620 (2023).
21. Y. Y. Zhou, L. Zhang, W. Z. Wang, Direct functionalization of methane into ethanol over copper modified polymeric carbon nitride via photocatalysis. *Nat. Commun.* **10**, 506 (2019).
22. X. Song, C. Basheer, R. N. Zare, Water microdroplets-initiated methane oxidation. *J. Am. Chem. Soc.* **145**, 27198–27204 (2023).
23. P. Zhou *et al.*, Water-promoted selective photocatalytic methane oxidation for methanol production. *Chem. Sci.* **15**, 1505–1510 (2024).
24. Y. Wang, Y. Zhang, X. Wang, Y. Liu, Z. Wu, Photothermal direct methane conversion to formaldehyde at the gas-solid interface under ambient pressure. *Nat. Commun.* **16**, 2550 (2025).
25. Y. Hao *et al.*, Continuous photo-oxidation of methane to methanol at an atomically tailored reticular gas-solid interface. *Nat. Commun.* **16**, 747 (2025).
26. Y. Y. Fan *et al.*, Selective photocatalytic oxidation of methane by quantum-sized bismuth vanadate. *Nat. Sustain.* **4**, 509–515 (2021).
27. Y. Lin, H. Hu, Y. H. Hu, Role of ZnO morphology in its reduction and photocatalysis. *Appl. Surf. Sci.* **502**, 144202 (2020).
28. Z. G. Geng *et al.*, Oxygen vacancies in ZnO nanosheets enhance CO_2 electrochemical reduction to CO. *Angew. Chem. Int. Ed. Engl.* **57**, 6054–6059 (2018).
29. T. Y. Song *et al.*, Enhanced methanol synthesis over self-limited ZnO overlayers on Cu nanoparticles formed via gas-phase migration route. *Angew. Chem. Int. Ed. Engl.* **63**, e202316888 (2024).
30. H. Y. Yuan *et al.*, ZnO nanosheets abundant in oxygen vacancies derived from metal-organic frameworks for ppb-level gas sensing. *Adv. Mater.* **31**, 1807161 (2019).
31. G. Ou *et al.*, Tuning defects in oxides at room temperature by lithium reduction. *Nat. Commun.* **9**, 1302 (2018).
32. M. D. Argyle, C. H. Bartholomew, Heterogeneous catalyst deactivation and regeneration: A review. *Catalysts* **5**, 145–269 (2015).
33. F. Lin *et al.*, Catalyst deactivation and its mitigation during catalytic conversions of biomass. *ACS Catal.* **12**, 13555–13599 (2022).
34. E. T. C. Vogt, D. L. Fu, B. M. Weckhuysen, Carbon deposit analysis in catalyst deactivation, regeneration, and rejuvenation. *Angew. Chem. Int. Ed. Engl.* **62**, e202300319 (2023).
35. X. X. Chen *et al.*, Photocatalytic oxidation of methane over silver decorated zinc oxide nanocatalysts. *Nat. Commun.* **7**, 12273 (2016).
36. D. Wang, Z.-P. Liu, W.-M. Yang, Proton-promoted electron transfer in photocatalysis: Key step for photocatalytic hydrogen evolution on metal/titania composites. *ACS Catal.* **7**, 2744–2752 (2017).
37. T. Hiramatsu *et al.*, Correlation between crystallinity and oxygen vacancy formation in In-Ga-Zn oxide. *Jpn. J. Appl. Phys.* **55**, 021203 (2016).
38. S. H. Yan *et al.*, Research advances of amorphous metal oxides in electrochemical energy storage and conversion. *Small* **15**, 1804371 (2019).
39. W. X. Ouyang, F. Teng, J. H. He, X. S. Fang, Enhancing the photoelectric performance of photodetectors based on metal oxide semiconductors by charge-carrier engineering. *Adv. Funct. Mater.* **29**, 1807672 (2019).
40. N. D. Feng *et al.*, Efficient and selective photocatalytic CH_4 conversion to CH_3OH with O by controlling overoxidation on TiO_2. *Nat. Commun.* **12**, 4652 (2021).
41. G. L. Chiarello, D. Ferri, E. Selli, In situ attenuated total reflection infrared spectroscopy study of the photocatalytic steam reforming of methanol on Pt/TiO_2. *Appl. Surf. Sci.* **450**, 146–154 (2018).
42. P. K. Huttunen *et al.*, DRIFTS investigation of methanol oxidation on CeO_2 nanoparticles. *Appl. Surf. Sci.* **554**, 149518 (2021).
43. E. M. Wilcox, G. W. Roberts, J. J. Spivey, Direct catalytic formation of acetic acid from CO and methane. *Catal. Today* **88**, 83–90 (2003).
44. W. B. Jiang *et al.*, Pd-modified ZnO-Au enabling alkoxy intermediates formation and dehydrogenation for photocatalytic conversion of methane to ethylene. *J. Am. Chem. Soc.* **143**, 269–278 (2021).
45. G. Kim, G. Kwon, H. Lee, The role of surface hydroxyl groups on a single-atomic Rh_1/ZrO_2 catalyst for direct methane oxidation. *Chem. Commun.* **57**, 1671–1674 (2021).
46. J. J. Chen *et al.*, Mechanistic understanding of methane combustion over Ni/CeO_2: A combined experimental and theoretical approach. *ACS Catal.* **11**, 9345–9354 (2021).
47. I. Friberg, N. Sadokhina, L. Olsson, Complete methane oxidation over Ba modified Pd/Al_2O_3: The effect of water vapor. *Appl. Catal. B-Environ.* **231**, 242–250 (2018).
48. D. Mora-Fonz *et al.*, Why are polar surfaces of ZnO stable? *Chem. Mater.* **29**, 5306–5320 (2017).
49. F. W. Campbell, S. R. Belding, R. Baron, L. Xiao, R. G. Compton, The hydrogen evolution reaction at a silver nanoparticle array and a silver macroelectrode compared: Changed electrode kinetics between the macro- and nanoscales. *J. Phys. Chem. C* **113**, 14852–14857 (2009).
50. Y. Hu *et al.*, Enhanced photoelectrochemical hydrogen evolution on CuBi2O4 photocathode with silver as conductive channels. *Catal. Lett.* **154**, 34–41 (2024).